Kardar–Parisi–Zhang universality in a one-dimensional polariton condensate

https://doi.org/10.1038/s41586-022-05001-8

Received: 16 December 2021

Accepted: 21 June 2022

Published online: 24 August 2022

Check for updates

Quentin Fontaine[1], Davide Squizzato[2,3,4], Florent Baboux[1,5], Ivan Amelio[6], Aristide Lemaître[1], Martina Morassi[1], Isabelle Sagnes[1], Luc Le Gratiet[1], Abdelmounaim Harouri[1], Michiel Wouters[7], Iacopo Carusotto[6], Alberto Amo[8], Maxime Richard[9], Anna Minguzzi[2], Léonie Canet[2]✉, Sylvain Ravets[1] & Jacqueline Bloch[1]✉

Revealing universal behaviours is a hallmark of statistical physics. Phenomena such as the stochastic growth of crystalline surfaces[1] and of interfaces in bacterial colonies[2], and spin transport in quantum magnets[3–6] all belong to the same universality class, despite the great plurality of physical mechanisms they involve at the microscopic level. More specifically, in all these systems, space–time correlations show power-law scalings characterized by universal critical exponents. This universality stems from a common underlying effective dynamics governed by the nonlinear stochastic Kardar–Parisi–Zhang (KPZ) equation[7]. Recent theoretical works have suggested that this dynamics also emerges in the phase of out-of-equilibrium systems showing macroscopic spontaneous coherence[8–17]. Here we experimentally demonstrate that the evolution of the phase in a driven-dissipative one-dimensional polariton condensate falls in the KPZ universality class. Our demonstration relies on a direct measurement of KPZ space–time scaling laws[18,19], combined with a theoretical analysis that reveals other key signatures of this universality class. Our results highlight fundamental physical differences between out-of-equilibrium condensates and their equilibrium counterparts, and open a paradigm for exploring universal behaviours in driven open quantum systems.

Universality is a powerful concept in statistical physics that allows the description of critical phenomena on the basis of a few fundamental ingredients. At thermal equilibrium, models such as the Ising model are pivotal in understanding the critical properties of a wide class of physical systems. However, non-equilibrium systems lack a complete classification of their universal properties. In this context, the Kardar–Parisi–Zhang (KPZ) equation appears as a quintessential model to investigate non-equilibrium phenomena and phase transitions. Here we provide an experimental demonstration that one-dimensional (1D) out-of-equilibrium condensates belong to the KPZ universality class.

The KPZ equation[7] was originally proposed to describe the stochastic growth dynamics of an interface height $h(\mathbf{r},t)$:

$$\partial_t h(\mathbf{r},t)=\nu\nabla^2 h(\mathbf{r},t)+\frac{\lambda}{2}[\nabla(h(\mathbf{r},t))]^2+\eta(\mathbf{r},t), \tag{1}$$

where $\mathbf{r}$ is the position vector, t the time coordinate, ∇ the gradient operator, while ν and λ are model parameters. The first term on the right corresponds to a smoothening diffusion, the second term corresponds to a nonlinear contribution leading to critical roughening, and $\eta(\mathbf{r},t)$ is a Gaussian white noise introducing stochasticity. The spatial and temporal correlation functions of $h(\mathbf{r},t)$ exhibit power-law behaviours, with critical exponents specific to the KPZ universality class[7]. Currently available observations of KPZ dynamics have mainly focused on growing interfaces in classical systems[19–21] and lately in quantum magnets[3–6].

Recent theoretical works have predicted that the spatio-temporal evolution of the phase of a polariton condensate falls into the KPZ universality class[8–17]. However, unlike an actual interface height, the phase is defined periodically between 0 and 2π. This version of the KPZ equation is relevant for out-of-equilibrium systems developing macroscopic spontaneous coherence (lasers and arrays of coupled limit-cycle oscillators[22]), and also for polar active smectic phases[23]. The compactness of the phase field results in a rich phase diagram comprising not only the KPZ phase but also other regimes characterized by the proliferation of topological defects[22–24]. Here we experimentally explore the spatio-temporal dynamics of the first-order coherence in a 1D polariton condensate. We observe the predicted coherence decay, and demonstrate the collapse of the data onto the universal KPZ scaling function. Our theoretical analysis shows how the observed 1D KPZ physics is resilient to the presence of vortex–antivortex (V–AV) pairs.

One-dimensional polariton condensates

Cavity polaritons are hybrid quasiparticles emerging in semiconductor cavities from the strong coupling between electronic excitations (excitons) in a quantum well and cavity photons[25]. Polaritons can be

---

[1]Université Paris-Saclay, CNRS, Centre de Nanosciences et de Nanotechnologies (C2N), Palaiseau, France. [2]Université Grenoble Alpes and CNRS, Laboratoire de Physique et Modélisation des Milieux Condensés (LPMMC), Grenoble, France. [3]Dipartimento di Fisica, Università La Sapienza, Rome, Italy. [4]Istituto Sistemi Complessi, Consiglio Nazionale delle Ricerche, Università La Sapienza, Rome, Italy. [5]Laboratoire Matériaux et Phénomènes Quantiques, Université de Paris, CNRS-UMR 7162, Paris, France. [6]INO-CNR BEC Center and Dipartimento di Fisica, Università di Trento, Povo, Italy. [7]TQC, Universiteit Antwerpen, Antwerp, Belgium. [8]Univ. Lille, CNRS, UMR 8523 - PhLAM - Physique des Lasers Atomes et Molécules, Lille, France. [9]Université Grenoble Alpes, CNRS, Grenoble INP, Institut Néel, Grenoble, France. ✉e-mail: leonie.canet@lpmmc.cnrs.fr; jacqueline.bloch@c2n.upsaclay.fr

created from a gain medium of incoherent excitons (the excitonic reservoir) through bosonic stimulated scattering. Owing to photon leakage through the mirrors, the polariton dynamics is intrinsically out of equilibrium, its steady state being the result of the balance between drive, relaxation and losses. Finally, polaritons can be laterally confined in lattices[26], enabling band-structure engineering.

The 1D polariton condensates at play consist of the macroscopic occupation of a given state obtained by incoherently pumping the exciton reservoir[27,28]. Above a critical density, exciton stimulated scattering from the reservoir into this state triggers a spontaneous U(1) symmetry-breaking of the phase. The condensate and reservoir dynamics are described by two coupled equations[25]:

$$i\hbar\frac{\partial}{\partial t}\psi(x,t) = \left[E(\hat{k}) - \frac{i\hbar}{2}\gamma(\hat{k}) + g|\psi(x,t)|^2 + 2g_R n_R(x,t) + \frac{i\hbar}{2}Rn_R(x,t)\right]\psi(x,t) + \xi(x,t) \qquad (2)$$

$$\frac{\partial}{\partial t}n_R(x,t) = P(x) - \left(\gamma_R + R\left|\psi(x,t)\right|^2\right)n_R(x,t) \qquad (3)$$

Here, x and t are the space and time coordinates, $\hat{k} = -i\hbar\partial/\partial x$ is the momentum operator, $\psi(x,t) = \sqrt{\rho(x,t)}\ e^{i\theta(x,t)}$ the polariton condensate field with density $\rho(x,t)$ and phase $\theta(x,t)$, $E(\hat{k})$ is the polariton dispersion, $\gamma(\hat{k})$ is the momentum-dependent decay rate, g is the polariton–polariton interaction strength and $\hbar$ is the reduced Planck constant. The exciton reservoir, with density $n_R(x,t)$, is pumped at rate $P(x)$. Excitons either relax into the polariton condensate by stimulated scattering with rate R or decay following other channels at rate γ_R. The term $2g_R n_R$ describes the polariton repulsive interactions with reservoir excitons (g_R being the exciton–exciton interaction strength). It dominates the polariton blueshift close to the threshold, and induces dephasing through inhomogeneous spectral broadening[29]. Finally, $\xi(x,t)$ describes the Gaussian noise induced by drive and loss.

Ignoring interactions with the reservoir ($g_R = 0$), previous theoretical studies have shown that the condensate phase $\theta(x,t)$ follows a KPZ equation[8–10]. The condensate phase profile behaves as a classical interface (Fig. 1a), and develops KPZ spatio-temporal correlations characterized by the phase variance $\mathrm{Var}(\Delta\theta(x,t)) = \langle(\Delta\theta(x,t) - \langle\Delta\theta(x,t)\rangle)^2\rangle$ (where $\langle.\rangle$ stands for statistical averaging, and $\Delta\theta = \theta(x,t) - \theta(x,t_0)$, t_0 being a reference time). Here we derive the mapping to the KPZ equation for $g_R \neq 0$ and obtain the KPZ parameters in terms of those entering equations (2) and (3) (Supplementary Information).

Experimentally probing KPZ correlations requires extended condensates to avoid finite size effects, a condition that was not fulfilled in early coherence measurements[30,31]. This requirement is demanding owing to the development of a modulation instability, which fragments the condensate into mutually incoherent micrometre-sized puddles[32–35]. Indeed, repulsive condensate–reservoir interactions result in effective attractive polariton–polariton interactions within the condensate and lead to its destabilization[36,37]. A solution to tame this instability is to spatially separate the excitonic reservoir from the condensate[38], or to use negative-mass polaritons in a lattice[39]. The negative mass changes the sign of the effective polariton–polariton interactions, thus restoring the condensate stability. Using this negative-mass technique, we generate stable 1D polariton condensates extending over more than 100 μm (Fig. 1b).

The sample consists of a semiconductor microcavity embedding quantum wells (Fig. 1c and Supplementary Information). We use nanotechnology processes to fabricate 1D asymmetric Lieb lattices of coupled micropillars containing three sites per unit cell (Fig. 1c, Methods and Supplementary Information). We incoherently populate the excitonic reservoir using a blue-detuned continuous-wave laser focused on a single lattice, with an elongated flat-top intensity profile.

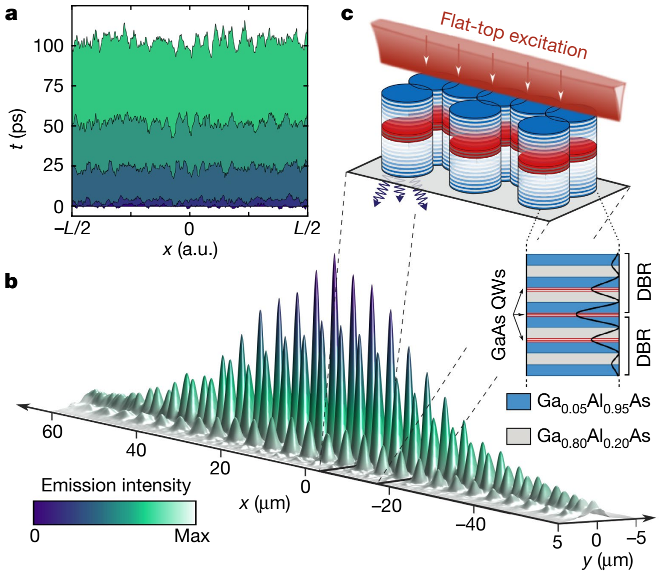

Fig. 1 | KPZ physics in the phase dynamics of a 1D polariton condensate. **a**, Snapshots of the condensate phase evolution obtained by numerically solving equations (2) and (3). The unwrapped phase evolves over time as a growing interface. **b**, Intensity distribution of the condensate emission measured for $P/P_{th} = 1.1$. **c**, Sketch of the lattice together with the excitation scheme. The lattice is excited using an elongated flat-top beam. Inset: sketch of a micropillar inner structure. A semiconductor optical microcavity is enclosed by two distributed Bragg reflectors (DBR). Quantum wells (QWs, red layers) are distributed at the anti-nodes of the cavity mode (black line).

The polariton emission analysed in momentum space below the condensation threshold (Fig. 2a) shows the lattice band structure emerging from the hybridization of the discrete modes confined in each micropillar. Above a power threshold $P_{th} = 50$ mW, the emission peaks at the top of the negative-mass band (Fig. 2b). This feature, together with the nonlinear increase of the emission intensity (Fig. 2c), indicates the onset of polariton condensation. The condensate emission intensity in real space at power $P = 1.1P_{th}$ reveals an extended and regular intensity profile envelope (Fig. 1b).

KPZ scaling in the condensate coherence decay

We define the first-order correlation evaluated between points separated in space by $\Delta x = 2x$ and delayed by Δt:

$$g^{(1)}(\Delta x,\Delta t) = \frac{\langle\psi^*(x,t_0)\psi(-x,t_0+\Delta t)\rangle}{\sqrt{\langle|\psi(x,t_0)|^2\rangle}\sqrt{\langle|\psi(-x,t_0+\Delta t)|^2\rangle}}. \qquad (4)$$

Neglecting density–density and density–phase correlations, we show that $g^{(1)}(\Delta x,\Delta t) \approx \exp\{-\mathrm{Var}[\Delta\theta(\Delta x,\Delta t)]/2\}$ (Supplementary Information). We thus expect KPZ universal scaling to show up as stretched exponentials in the coherence decay: $|g^{(1)}(\Delta x,0)| \propto \exp[-(\Delta x/\lambda)^{2\chi}/2]$ and $|g^{(1)}(0,\Delta t)| \propto \exp[-(\Delta t/\tau)^{2\beta}/2]$, where χ and β are the universal KPZ critical exponents and λ and τ are two non-universal parameters. In one dimension, the 'roughness' exponent χ is equal to 1/2 and the 'growth' exponent β is equal to 1/3 (refs. [18,19]). Although $\chi = 1/2$ is common to several universality classes for 1D systems (such as Edwards–Wilkinson[40]), $\beta = 1/3$ is an unambiguous signature of KPZ physics.

The condensate coherence $|g^{(1)}|$ measured by Michelson interferometry (Fig. 2d and Methods for details) is reported in Fig. 2e. We first focus on the temporal decay of the coherence. To search for the growth exponent, we calculate the temporal derivative $\mathcal{D}_t = -2\,\partial\log(|g^{(1)}(0,\Delta t)|)/\partial\Delta t$ from our dataset. According to KPZ theory, this derivative scales as a power law with exponent $2\beta - 1 = -1/3$.

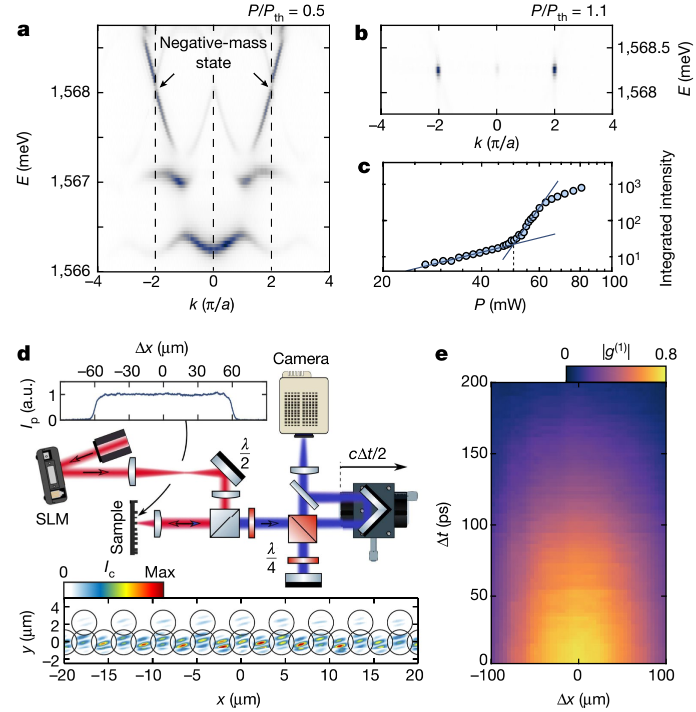

Fig. 2 | Probing the coherence of 1D polariton condensates. a,**b**, Momentum-resolved emission spectra captured below ($P/P_{th} = 0.5$; **a**) and above ($P/P_{th} = 1.1$; **b**) the condensation threshold. The horizontal and vertical axis are the polariton wave-vector k and energy E respectively. Above the threshold, the emission peaks at the top of the third band, showing polariton condensation in a negative-mass state. **c**, Integrated emission intensity as a function of the excitation power. The onset of the intensity nonlinear increase is observed for $P_{th} \approx 50$ mW. **d**, Sketch of the experimental set-up. SLM, spatial light modulator. Top inset: flat-top intensity profile I_p of the excitation spot. Bottom inset: the interference pattern obtained for $P/P_{th} = 1.13$ by overlapping the condensate field $\mathcal{E}(x, t_0)$ with its mirror symmetric $\mathcal{E}(-x, t_0)$ ($\Delta t = 0$). The black circles indicate the lattice pillars. The resulting intensity pattern exhibits well contrasted interference fringes over the whole condensate, indicating extended spatial coherence. I_c, condensate intensity. **e**, Coherence map showing the value of $|g^{(1)}|$, retrieved from the fringe visibility using equation (5), as a function of Δx and Δt.

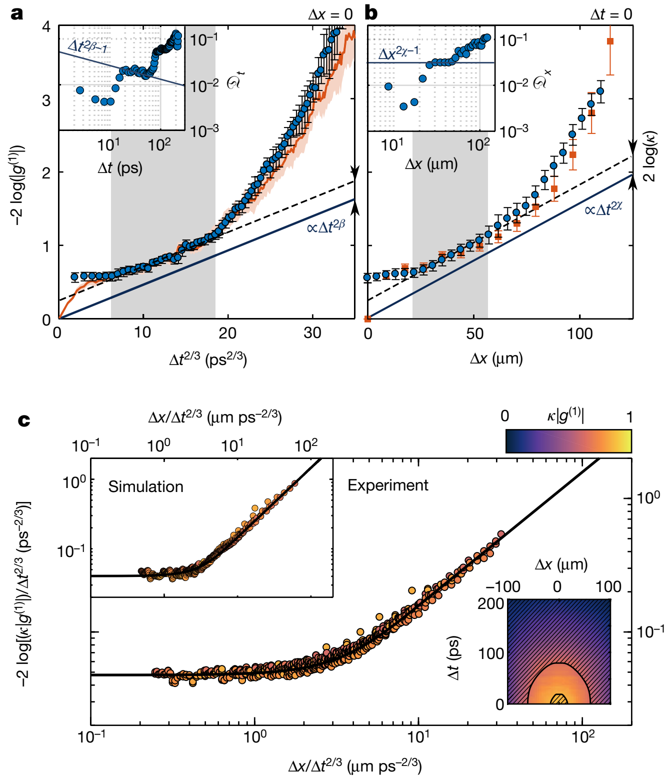

Fig. 3 | KPZ scaling in the coherence decay of a 1D polariton condensate. **a**, Measured values of $-2\log(|g^{(1)}(0, \Delta t)|)$ as a function of $\Delta t^{2/3}$. Inset: temporal derivative of $-2\log(|g^{(1)}(0, \Delta t)|)$, calculated from the experimental data, as a function of Δt. **b**, Measured values of $-2\log(|g^{(1)}(\Delta x, 0)|)$ as a function of Δx. Inset: spatial derivative of $-2\log(|g^{(1)}(\Delta x, 0)|)$, calculated from the experimental data, as a function of Δx. In both panels, the grey area delimits the KPZ window. In **a** (**b**), the simulated data are shown with an orange line (squares). Error bars on the experimental data points are calculated by performing a repeatability analysis on the numerical extraction of $g^{(1)}(\Delta x, \Delta t)$ from the interferograms. The orange-shaded area (orange error bars) in **a** (**b**) shows the 95% confidence interval on the simulated data. **c**, Measured values of $-2\log(\kappa|g^{(1)}|)/\Delta t^{2/3}$ as a function of $y = \Delta x/\Delta t^{2/3}$, for points within the non-hatched region of the coherence map (bottom inset). Top inset: the same as in the main panel but for numerical data. In both graphs, the black line corresponds to the KPZ scaling function $F = C_0 F_{KPZ}(y/y_0)$, adjusted to the experimental data by tuning the values of C_0 and y_0. Experimental and simulated $|g^{(1)}|$ datasets are normalized using $\kappa = 1.13$. In all panels, the numerical data are averaged over 10^4 realizations of the noise.

In the inset of Fig. 3a, we identify such scaling throughout the temporal window 15 ps ≤ Δt ≤ 80 ps. Equivalently, we observe in the main panel a linear increase of $-2\log(|g^{(1)}(0, \Delta t)|)$ as a function of $\Delta t^{2/3}$ over the same window (grey shaded area), which demonstrates a key feature of KPZ dynamics. At short timescales, the deviation from KPZ scaling and the saturation of $|g^{(1)}|$ are due to an incoherent background (spectrally broad photoluminescence from uncondensed states) that hides the onset of KPZ fluctuations. For $\Delta t \geq 80$ ps, $-2\log(|g^{(1)}(0, \Delta t)|)$ also departs from KPZ scaling and follows a super-linear behaviour that we attribute to slow reservoir population fluctuations[29]. We now perform a similar analysis in the spatial domain. The results are shown in Fig. 3b. The spatial derivative $\mathcal{D}_x = -2\,\partial\log(|g^{(1)}(\Delta x, 0)|)/\partial\Delta x$ exhibits a plateau within the spatial window 30 μm ≤ Δx ≤ 60 μm, in agreement with $\chi = 1/2$ (inset). The roughness exponent $\chi = 1/2$ also shows up in the linear increase of $-2\log(|g^{(1)}(\Delta x, 0)|)$, over the same window (grey shaded area in the main panel). When approaching condensate edges (Δx ≥ 60 μm), the coherence decays faster because of enhanced fluctuations at smaller polariton density. Pushing further this data analysis, we fit the coherence decay curves with stretched exponentials and deduce experimental values for the scaling exponents: $\chi_{exp} = 0.51 \pm 0.08$ and $\beta_{exp} = 0.36 \pm 0.11$. The uncertainty on β_{exp} allows us to discriminate between the different universality classes relevant for our system, as the KPZ value $\beta = 1/3$ remains the only one lying within the 95% confidence interval on β_{exp} (Supplementary Information).

We now search for KPZ signatures over the whole space–time correlation map. We select all data points where $0.57 \leq |g^{(1)}| \leq 0.75$, the range where we evidence KPZ scaling at Δt = 0. This space–time window is shown in the bottom inset of Fig. 3c. For this subset of data points, we plot in Fig. 3c the value of $-2\log(\kappa|g^{(1)}(\Delta x, \Delta t)|)/\Delta t^{2\beta}$ as a function of the rescaled coordinate $y = \Delta x/\Delta t^{2/3}$, where κ is a normalization factor (Supplementary Information). Strikingly, all these data points collapse onto the scaling function $F = C_0 F_{KPZ}(y/y_0)$, where F_{KPZ} is the tabulated dimensionless KPZ universal scaling function[41]. We use the non-universal constants C_0 and y_0 as fitting parameters to overlap F with the collapsed data points. This result demonstrates that 1D polariton condensates indeed belong to the KPZ universality class. To reinforce the generality of this conclusion, we performed the same measurement and analysis on a different 1D lattice with four sites per unit cell. We also found a KPZ space–time window where all data points collapse onto the universal scaling curve (Supplementary Information).

To complete the picture, we carried out the same analysis at higher excitation powers, and found for both lattices that the spatio-temporal KPZ window shrinks for increasing P/P_{th} and eventually disappears when $P/P_{\mathrm{th}} > 1.2$ (Supplementary Information).

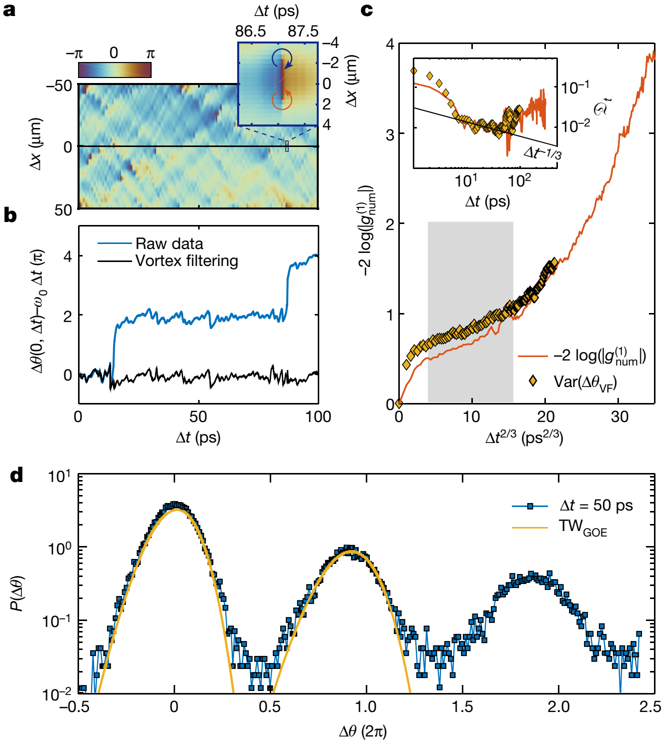

Fig. 4 | Analysis of the simulated phase dynamics. a, Example of a phase map. For better visualization, we plot the wrapped phase after subtracting the linear phase evolution $\omega_0 \Delta t$ ($\hbar\omega_0$ being the condensate energy). Inset: zoom on a V–AV pair. **b**, Time evolution of the unwrapped phase along $x = 0$ (blue line): two V–AV pairs are crossed, resulting in two phase jumps of approximately 2π. The black line in **b** is obtained by filtering all the vortices present in the phase map (**a**). **c**, $-2\log|g^{(1)}|$ (red line) and $\mathrm{Var}(\Delta\theta_{\mathrm{VF}})$ (symbols) as a function of $\Delta t^{2/3}$ for $\Delta x = 0$, computed over 10^4 realizations. The orange line is the same as in Fig. 3a. Inset: temporal derivative of $-2\log(|g^{(1)}|)$ (red line) and $\mathrm{Var}(\Delta\theta_{\mathrm{VF}})$ (symbols) as a function of Δt, showing similar behaviour in the KPZ window. **d**, Probability distribution of phase fluctuations obtained at $\Delta t = 50$ ps (blue squares) from numerical simulations. Our computation involves 3×10^4 realizations of the noise. The first (second, third and so on) peak from the left gathers the realizations for which no jump (one, two and so on) has occurred before $\Delta t = 50$ ps. Yellow line: fit of the numerical data by the Tracy–Widom (TW) GOE distribution.

Resilience of KPZ physics to space–time vortices

To numerically reproduce these experimental data, we calculate the phase evolution of the polariton condensate by numerically solving equations (2) and (3). Details about how we set the simulation parameters can be found in Methods. It is noted that we neglect the polariton–polariton interaction energy $g|\psi|^2$ and take $g = 0$ in all simulations. As such, this model also applies to spatially extended lasers in the weak coupling regime. The calculated $|g^{(1)}_{\mathrm{num}}|$ data are reported in Fig. 3a,b, showing excellent agreement with the experiment. The short- and long-time behaviour is reproduced, together with the shrinking of the KPZ window when the excitation power is increased (Supplementary Information).

We then perform on the numerical data the same analysis as on the experimental data. We plot $-2\log(\kappa|g^{(1)}_{\mathrm{num}}(\Delta x, \Delta t)|)/\Delta t^{2\beta}$ as a function of y, selecting the points for which $0.57 \le |g^{(1)}_{\mathrm{num}}| \le 0.75$. The result is shown in Fig. 3c (top inset), together with the KPZ scaling function $F = C_0 F_{\mathrm{KPZ}}(y/y_0)$, using for C_0 and y_0 the same values as for the experimental data. The simulated data align to the scaling function, thus fully validating our model.

To deepen our insight into the phase dynamics, we now analyse its stochastic behaviour in the numerical simulations. Figure 4a shows an example of a phase map $\Delta\theta(x, \Delta t)$ corresponding to a given realization of the noise (others are shown in Supplementary Information). We observe two kinds of phase variation: small-amplitude fluctuations and fast (scarce) phase jumps. These jumps are associated with pairs of close-by spatio-temporal vortices with opposite circulation (see inset), that we name V–AV pairs. To analyse their effect on the phase dynamics, we show in Fig. 4b the unwrapped phase temporal evolution at $x = 0$ (horizontal line in Fig. 4a). The phase evolution exhibits plateaus with small-amplitude phase fluctuations, separated by phase jumps of approximately 2π, occurring on a fast timescale (about 1 ps) when passing through a V–AV pair. It is noted that for the regime of parameters explored here, almost all vortices appear in V–AV pairs. For higher noise or stronger interactions, activation of single vortices is expected and would lead to other dynamical regimes[24].

We now show that small-amplitude phase fluctuations follow KPZ scaling laws by computing the phase variance $\mathrm{Var}(\Delta\theta)$. As this quantity is extremely sensitive to phase jumps, we filter them out in the calculation (Methods). The result is plotted in Fig. 4c together with the values of $-2\log(|g^{(1)}_{\mathrm{num}}|)$ (calculated without filtering the V–AV pairs). Both quantities exhibit the KPZ power-law scaling over the same time window (grey shaded area), as further illustrated in Fig. 4c (inset) where we plot their time derivative. This result definitely confirms that the first-order coherence is a good observable to probe the KPZ dynamics of the condensate phase, even in the presence of few V–AV pairs.

Another striking signature of KPZ physics lies in the fact that phase fluctuations are governed by a probability distribution, which—unlike the normal distribution—is skewed and exhibits markedly different tails. In Fig. 4d, we show the calculated probability distribution of the unwrapped $\Delta\theta(0, \Delta t)$, computed over all trajectories (thus including vortices) for $\Delta t = 50$ ps, that is, in the centre of the KPZ window. All trajectories that have not crossed any V–AV pair contribute to the first peak in the distribution. The second peak corresponds to trajectories that have crossed one V–AV pair before reaching $\Delta t = 50$ ps and have thus undergone one phase jump close to 2π. Strikingly the first two peaks are skewed and well reproduced by the Tracy–Widom Gaussian orthogonal ensemble (GOE) distribution associated with the flat subclass (Supplementary Information). Cumulating data for various Δt, we obtain an agreement with the Tracy–Widom GOE distribution over six decades (see Supplementary Information for details on the analysis). The third peak corresponds to few realizations showing two phase jumps. The lack of statistics prevents precise analysis of its shape. Our simulations highlight that V–AV pairs only modify the probability distribution by adding replicas of the main peak without significantly changing their shape. Moreover, they confirm that in the regime where a low density of V–AV pairs stochastically shows up, KPZ dynamics is not destroyed but occurs piece-wise in the spatio-temporal domain.

To conclude, both our experimental and theoretical analysis prove that KPZ scaling laws are present in the decay of the first-order coherence of 1D driven-dissipative polariton condensates. Our findings apply to any spatially extended driven open systems subject to gain and loss and characterized by a U(1) symmetry-breaking. Our work opens many challenges to be addressed in the future. In 1D, although our results highlight the striking resilience of KPZ physics to V–AV pairs, regimes at higher noise strength or higher nonlinearity remain to be explored[24]. Investigating different KPZ universality subclasses, predicted for various geometries of the unwrapped phase profile[16], is now also within reach, through engineering the geometry of the condensate environment. Beyond 1D, exciton–polariton lattices offer exciting perspectives for the exploration of KPZ physics in 2D, where an experimental realization is highly sought after[11–16], and the role of topological defects still actively debated[11]. An experimental implementation involving polariton condensates would enable testing of the different models and serve as a general testbed for exploring complex physical systems belonging to the KPZ universality class.

Online content

Any methods, additional references, Nature Research reporting summaries, source data, extended data, supplementary information, acknowledgements, peer review information; details of author contributions and competing interests; and statements of data and code availability are available at https://doi.org/10.1038/s41586-022-05001-8.

1. Krug, J. & Meakin, P. Universal finite-size effects in the rate of growth processes. *J. Phys. A* **23**, L987 (1990).
2. Wakita, J.-i, Itoh, H., Matsuyama, T. & Matsushita, M. Self-affinity for the growing interface of bacterial colonies. *J. Phys. Soc. Jpn* **66**, 67–72 (1997).
3. Ljubotina, M., Žnidarič, M. & Prosen, T. Spin diffusion from an inhomogeneous quench in an integrable system. *Nat. Commun.* **8**, 16117 (2017).
4. Ljubotina, M., Žnidarič, M. & Prosen, T. Kardar–Parisi–Zhang physics in the quantum Heisenberg magnet. *Phys. Rev. Lett.* **122**, 210602 (2019).
5. Scheie, A. et al. Detection of Kardar–Parisi–Zhang hydrodynamics in a quantum Heisenberg spin-1/2 chain. *Nat. Phys.* **17**, 726–730 (2021).
6. Wei, D. et al. Quantum gas microscopy of Kardar–Parisi–Zhang superdiffusion. *Science* **376**, 716–720 (2022).
7. Kardar, M., Parisi, G. & Zhang, Y.-C. Dynamic scaling of growing interfaces. *Phys. Rev. Lett.* **56**, 889–892 (1986).
8. Altman, E., Sieberer, L. M., Chen, L., Diehl, S. & Toner, J. Two-dimensional superfluidity of exciton polaritons requires strong anisotropy. *Phys. Rev. X* **5**, 011017 (2015).
9. Ji, K., Gladilin, V. N. & Wouters, M. Temporal coherence of one-dimensional nonequilibrium quantum fluids. *Phys. Rev. B* **91**, 045301 (2015).
10. He, L., Sieberer, L. M., Altman, E. & Diehl, S. Scaling properties of one-dimensional driven-dissipative condensates. *Phys. Rev. B* **92**, 155307 (2015).
11. Zamora, A., Sieberer, L., Dunnett, K., Diehl, S. & Szymańska, M. Tuning across universalities with a driven open condensate. *Phys. Rev. X* **7**, 041006 (2017).
12. Comaron, P. et al. Dynamical critical exponents in driven-dissipative quantum systems. *Phys. Rev. Lett.* **121**, 095302 (2018).
13. Squizzato, D., Canet, L. & Minguzzi, A. Kardar–Parisi–Zhang universality in the phase distributions of one-dimensional exciton–polaritons. *Phys. Rev. B* **97**, 195453 (2018).
14. Amelio, I. & Carusotto, I. Theory of the coherence of topological lasers. *Phys. Rev. X* **10**, 041060 (2020).
15. Ferrier, A., Zamora, A., Dagvadorj, G. & Szymańska, M. Searching for the Kardar–Parisi–Zhang phase in microcavity polaritons. *Phys. Rev. B* **105**, 205301 (2022)
16. Deligiannis, K., Squizzato, D., Minguzzi, A. & Canet, L. Accessing Kardar–Parisi–Zhang universality sub-classes with exciton polaritons. *Europhys. Lett.* **132**, 67004 (2021).
17. Mei, Q., Ji, K. & Wouters, M. Spatiotemporal scaling of two-dimensional nonequilibrium exciton–polariton systems with weak interactions. *Phys. Rev. B* **103**, 045302 (2021).
18. Family, F. & Vicsek, T. Scaling of the active zone in the eden process on percolation networks and the ballistic deposition model. *J. Phys. A* **18**, L75 (1985).
19. Halpin-Healy, T. & Zhang, Y.-C. Kinetic roughening phenomena, stochastic growth, directed polymers and all that. Aspects of multidisciplinary statistical mechanics. *Phys. Rep.* **254**, 215–414 (1995).
20. Krug, J. Origins of scale invariance in growth processes. *Adv. Phys.* **46**, 139–282 (1997).
21. Takeuchi, K. A. An appetizer to modern developments on the Kardar–Parisi–Zhang universality class. *Physica A* **504**, 77–105 (2018).
22. Lauter, R., Mitra, A. & Marquardt, F. From Kardar–Parisi–Zhang scaling to explosive desynchronization in arrays of limit-cycle oscillators. *Phys. Rev. E* **96**, 012220 (2017).
23. Chen, L. & Toner, J. et al. Universality for moving stripes: a hydrodynamic theory of polar active smectics. *Phys. Rev. Lett.* **111**, 088701 (2013).
24. He, L., Sieberer, L. M. & Diehl, S. Space–time vortex driven crossover and vortex turbulence phase transition in one-dimensional driven open condensates. *Phys. Rev. Lett.* **118**, 085301 (2017).
25. Carusotto, I. & Ciuti, C. Quantum fluids of light. *Rev. Mod. Phys.* **85**, 299–366 (2013).
26. Schneider, C. et al. Exciton–polariton trapping and potential landscape engineering. *Rep. Prog. Phys.* **80**, 016503 (2016).
27. Deng, H., Weihs, G., Santori, C., Bloch, J. & Yamamoto, Y. Condensation of semiconductor microcavity exciton polaritons. *Science* **298**, 199–202 (2002).
28. Kasprzak, J. et al. Bose–Einstein condensation of exciton polaritons. *Nature* **443**, 409–414 (2006).
29. Love, A. et al. Intrinsic decoherence mechanisms in the microcavity polariton condensate. *Phys. Rev. Lett.* **101**, 067404 (2008).
30. Roumpos, G. et al. Power-law decay of the spatial correlation function in exciton-polariton condensates. *Proc. Natl Acad. Sci.* **109**, 6467–6472 (2012).
31. Fischer, J. et al. Spatial coherence properties of one dimensional exciton–polariton condensates. *Phys. Rev. Lett.* **113**, 203902 (2014).
32. Bobrovska, N., Ostrovskaya, E. A. & Matuszewski, M. Stability and spatial coherence of nonresonantly pumped exciton-polariton condensates. *Phys. Rev. B* **90**, 205304 (2014).
33. Daskalakis, K. S., Maier, S. A. & Kéna-Cohen, S. Spatial coherence and stability in a disordered organic polariton condensate. *Phys. Rev. Lett.* **115**, 035301 (2015).
34. Estrecho, E. et al. Single-shot condensation of exciton polaritons and the hole burning effect. *Nat. Commun.* **9**, 2944 (2018).
35. Bobrovska, N., Matuszewski, M., Daskalakis, K. S., Maier, S. A. & Kéna-Cohen, S. Dynamical instability of a nonequilibrium exciton–polariton condensate. *ACS Photon.* **5**, 111–118 (2018).
36. Smirnov, L. A., Smirnova, D. A., Ostrovskaya, E. A. & Kivshar, Y. S. Dynamics and stability of dark solitons in exciton–polariton condensates. *Phys. Rev. B* **89**, 235310 (2014).
37. Liew, T. C. H. et al. Instability-induced formation and nonequilibrium dynamics of phase defects in polariton condensates. *Phys. Rev. B* **91**, 085413 (2015).
38. Caputo, D. et al. Topological order and thermal equilibrium in polariton condensates. *Nat. Mater.* **17**, 145–151 (2018).
39. Baboux, F. et al. Unstable and stable regimes of polariton condensation. *Optica* **5**, 1163–1170 (2018).
40. Edwards, S. F. & Wilkinson, D. The surface statistics of a granular aggregate. *Proc. R. Soc. Lond. A* **381**, 17–31 (1982).
41. Prähofer, M. & Spohn, H. Exact scaling functions for one-dimensional stationary kpz growth. *J. Stat. Phys.* **115**, 255–279 (2004).

Publisher's note Springer Nature remains neutral with regard to jurisdictional claims in published maps and institutional affiliations.

© The Author(s), under exclusive licence to Springer Nature Limited 2022

Methods

Experimental details

The sample used in this paper consists of a high-quality-factor ($Q \approx 70{,}000$) $\lambda/2$ $Ga_{0.05}Al_{0.95}As$ microcavity surrounded by two $Al_{0.20}Ga_{0.80}As$/$Al_{0.05}Ga_{0.95}As$ distributed Bragg reflectors. Three stacks of four 8-nm gallium arsenide (GaAs) quantum wells are embedded in this microstructure, at the anti-nodes of the cavity-mode electromagnetic field, resulting in a 15-meV collective Rabi splitting. The as-grown planar cavity is patterned into 1D lattices of coupled micropillars (3 µm in diameter), using electron beam lithography and dry etching. In this work, we use a 200-µm-long asymmetric Lieb lattice, made of three pillars per unit cell with 2.2-µm centre-to-centre separation distance. The sample is held at cryogenic temperature (4 K) in a closed-cycle cryostation.

We incoherently populate the excitonic reservoir using a non-resonant continuous-wave laser at 740 nm (reflectivity minimum of the Bragg mirror). A spatial light modulator enables shaping the excitation spot into a 125-µm-long flat-top beam in the lattice direction. It is noted that our experiment is performed under truly continuous-wave excitation conditions, that is, without any chopper. The polariton emission leaking out through the cavity top mirror is analysed in space, momentum (along the lattice direction x) and frequency with a monochromator coupled to a charge-coupled-device camera.

We retrieve the condensate first-order coherence using Michelson interferometry. A two-mirror retro-reflector mounted on a step-motorized translation stage in one of the interferometer arms enables overlapping on a charge-coupled-device camera the field $\mathcal{E}(x, t_0)$ emitted by the condensate at time t_0 and position x, with $\mathcal{E}(-x, t_0 + \Delta t)$, the field emitted at $t_0 + \Delta t$ and position $-x$ (Δt is the delay introduced between the interferometer arms by translating the retro-reflector). The fringe contrast gives a direct visualization of the degree of coherence between fields emitted at two points spatially separated by $\Delta x = 2x$ and delayed by Δt. More specifically, $|g^{(1)}(\Delta x, \Delta t)|$ is determined from the fringe visibility $V(\Delta x, \Delta t)$ and from the intensity distributions $|\mathcal{E}(x, t_0)|^2$ and $|\mathcal{E}(-x, t_0 + \Delta t)|^2$ measured separately, using

$$\begin{aligned} 2|g^{(1)}(\Delta x, \Delta t)|\sqrt{|\mathcal{E}(x, t_0)|^2|\mathcal{E}(-x, t_0 + \Delta t)|^2} \\ = V(\Delta x, \Delta t)\,[|\mathcal{E}(x, t_0)|^2 + |\mathcal{E}(-x, t_0 + \Delta t)|^2]. \end{aligned} \tag{5}$$

To probe the temporal scaling of the condensate coherence, we scan the retro-reflector position over $\Delta L = 5$ cm, corresponding to a maximum time delay of $\Delta t = 2\Delta L/c = 330$ ps (c being the speed of light in vaccum). During such a scan, we set the camera exposure time to 1 s and acquire a series of 250 images.

Integration method and parameters for numerical simulations

To compare our experimental findings to theory, we solved numerically the set of equations (2) and (3). The numerical integration of these equations is performed using the interaction picture method[42,43]. The idea behind this integration scheme is similar to the interaction picture in quantum mechanics. We first split equations (2) and (3) into a linear, exactly solvable part and a remaining nonlinear part. We then solve the linear component in Fourier space and transform it back to real space. We transform equations (2) and (3) by moving into the interaction picture and integrate the resulting nonlinear equation using semi-implicit Runge–Kutta method, with an adaptive time step. We take as the initial condition $\psi(x, t = 0) = 0$, and let the condensate grow under the action of the pumped reservoir. The sampling starts at t_0, long after the condensate has reached its stationary density profile. Usually, we perform our simulations using $t_0 = 10$ ns.

Some of the parameters entering the numerical simulations are known experimentally. For instance, we use a lattice spacing equal to the experimental lattice period $a = 4.4$ µm. The measurement of the polariton dispersion relation $E(k)$ (k being the polariton wave-vector) shown in Fig. 2a provides a good estimate of the polariton mass $m = -3.3 \times 10^{-6}\, m_e$ (m_e being the electron mass). The k-dependent polariton linewidth $\gamma(k)$ is modelled by the function

$$\gamma(k) = \gamma_0 + (\gamma_\infty - \gamma_0)\left[1 - \exp\left(-\frac{\gamma_2 k^2}{\gamma_\infty - \gamma_0}\right)\right] \tag{6}$$

which is compared with the experimental data in Supplementary Fig. 3d (blue solid line). The parameter values are $\gamma_{0,\mathrm{sim}} \equiv \gamma(k = 0) = 48.5$ µeV, $\gamma_{2,\mathrm{sim}} \equiv 1/2(\partial^2\gamma(k)/\partial k^2)|_{k=0} = 1.6 \times 10^4$ µeV µm^{-2} and $\gamma_{\infty,\mathrm{sim}} \equiv \lim k \to \infty \gamma(k) = 77$ µeV. Furthermore, the energy blueshift at threshold is known with good accuracy:

$$2\, g_R\, n_R|_{P=P_{th}} \approx 0.6\ \mathrm{meV} \equiv \mu_{th}, \tag{7}$$

where $n_R|_{P=P_{th}} = P_{th}/\gamma_R = \gamma_0/R$ stands for the reservoir density at condensation threshold and $P_{th} = \gamma_0\gamma_R/R$ for the threshold power. Assuming that g_R does not depend on the pumping power P, we find:

$$g_R = \frac{1}{2}\frac{\mu_{th} R}{\gamma_0}. \tag{8}$$

As the reservoir-induced blueshift $2g_R n_R$ is two orders of magnitude larger than the polariton-induced blueshift $g|\psi|^2$, we take $g = 0$ in our simulations. To qualitatively reproduce the spatial density profile of the condensate in our experiments, we use a spatially dependent flat-top pump profile modelled by

$$P(x) = P\,\frac{[1 + \tanh((L_0 + x)/\sigma)]\,[1 + \tanh((L_0 - x)/\sigma)]}{[1 + \tanh(L_0/\sigma)]^2} \tag{9}$$

where $L_0 = 80$ µm is the length of the pump spot and $\sigma = 9.7$ µm is the width of its decaying edges. The remaining free parameters in our numerical simulations are thus the scattering rate R of excitons into the condensate and the reservoir decay rate γ_R. For those parameters, we choose values within some realistic range yielding the best agreement with the measured $|g^{(1)}|$. All the simulations presented in this paper were performed using $\hbar R = 8.8 \times 10^{-4}$ µm ps^{-1} and $\gamma_R = 0.45\gamma_0$.

Calculation of the variance of the phase

To calculate Var ($\Delta\theta$), we select for each trajectory a 100-ps-wide window where the phase undergoes the smallest amount of jumps. When few phase jumps remain in the selected window, we filter them out by adding at every vortex location another one of opposite charge (black line in Fig. 4b). It is noted that we discard 5% of the realizations, where vortices proliferate (Supplementary Information). We then calculate the phase variance Var ($\Delta\theta_{VF}$) over the set of vortex-free (VF) time windows.

Data availability

All datasets generated and analysed during this study are available upon request from the corresponding authors. Source data are provided with this paper.

Code availability

All codes generated during this study are available upon request from the corresponding authors.

42. Dennis, G. R., Hope, J. J. & Johnsson, M. T. Xmds2: fast, scalable simulation of coupled stochastic partial differential equations. *Comput. Phys. Commun.* **184**, 201–208 (2013).
43. Werner, M. & Drummond, P. Robust algorithms for solving stochastic partial differential equations. *J. Comput. Phys.* **132**, 312–326 (1997).

Acknowledgements We thank V. Goblot, D. Vajner and A. Toor for their assistance in the early development of the experiment. This work was supported by the Paris Ile-de-France Région in the framework of DIM SIRTEQ, the French RENATECH network, the H2020-FETFLAG project PhoQus (820392), the QUANTERA project Interpol (ANR-QUAN-0003-05), the European Research Council via the project ARQADIA (949730), EmergenTopo (865151) and RG.BIO (785932), the French government through the Programme Investissement d'Avenir (I-SITE ULNE / ANR-16-IDEX-0004 ULNE) managed by the Agence Nationale de la Recherche, and the Labex CEMPI (ANR-11-LABX-0007). L.C. acknowledges support from ANR (grant ANR-18-CE92-0019) and from Institut Universitaire de France.

Author contributions Q.F. built the experimental set-up, performed the experiments and analysed the data. D.S. realized the theoretical calculations and numerical simulations. F.B. contributed to the design of the sample structure and initial characterization of the sample. A.L. and M.M. grew the sample by molecular beam epitaxy. I.S., L.L.G. and A.H. fabricated the polariton lattices. Q.F., D.S., I.A., M.W., I.C., A.A., M.R., A.M., L.C., S.R. and J.B. participated in the scientific discussions about all aspects of the work. Q.F., A.M., L.C., S.R. and J.B. wrote the original draft of the paper. Q.F., D.S., I.A., M.W., I.C., A.A., M.R., A.M., L.C., S.R. and J.B. reviewed and edited the paper into its current form. A.M., L.C., S.R. and J.B. supervised the work.

Competing interests The authors declare no competing interests.

Additional information

Supplementary information The online version contains supplementary material available at https://doi.org/10.1038/s41586-022-05001-8.

Correspondence and requests for materials should be addressed to Léonie Canet or Jacqueline Bloch.

Peer review information *Nature* thanks Sebastian Diehl, Michael Fraser and the other, anonymous, reviewer(s) for their contribution to the peer review of this work. Peer reviewer reports are available.

Reprints and permissions information is available at http://www.nature.com/reprints.